Carrier dynamics in a tunneling injection quantum dot semiconductor optical amplifier

I. Khanonkin* and G. Eisenstein
Andrew and Erna Viterbi Department of Electrical Engineering, Technion, Haifa 32000, Israel

M. Lorke, S. Michael, and F. Jahnke
Institute for Theoretical Physics, University of Bremen, 28334 Bremen, Germany

A. K. Mishra
School of Physical and Mathematical Sciences, Nanyang Technological University, Singapore 637371

J. P. Reithmaier
Institute of Nanostructure Technologies and Analytics, Technische Physik, CINSaT, University of Kassel, 34132 Kassel, Germany

(Received 19 July 2018; revised manuscript received 31 August 2018; published 14 September 2018)

The process of tunneling injection is known to improve the dynamical characteristics of quantum well and quantum dot lasers; in the latter, it also improves the temperature performance. The advantage of the tunneling injection process stems from the fact that it avoids hot carrier injection, which is a key performance-limiting factor in all semiconductor lasers. The tunneling injection process is not fully understood microscopically and therefore it is difficult to optimize those laser structures. We present here a numerical study of the broadband carrier dynamics in a tunneling injection quantum dot gain medium in the form of an optical amplifier operating at 1.55 μm. Charge carrier tunneling occurs in a hybrid state that joins the quantum dot first excited state and the confined quantum well–injection well states. The hybrid state, which is placed energetically roughly one longitudinal optic phonon above the ground state and has a spectral extent of about 5 meV, dominates the carrier injection to the ground state. We calculate the dynamical response of the inversion across the entire gain spectrum following a short pulse perturbation at various wavelengths and for two bias currents. At a high bias of 200 mA, the entire spectrum exhibits gain; at 30 mA, the system exhibits a mixed gain-absorption spectrum. The carrier dynamics in the injection well is calculated simultaneously. We discuss the role of the pulse excitation wavelengths relative to the gain spectrum peak and demonstrate that the injection well responds to all perturbation wavelengths, even those which are far from the region where the tunneling injection process dominates.

DOI: 10.1103/PhysRevB.98.125307

I. INTRODUCTION

The most basic mechanism limiting the modulation capabilities of semiconductor lasers is the gain nonlinearity, which originates from several processes including hot carrier injection [1–3]. An attractive way to diminish the hot carrier effect is to employ a delta-doped film near the active region [4] or a tunneling injection (TI) structure [5], which feeds cold carriers from an injection well (IW) reservoir directly to the lasing state. The successful use of TI was demonstrated for quantum well (QW) lasers more than 20 years ago [5] and later for quantum dot (QD) lasers at short wavelengths [6] as well as at 1550 nm [7]. The TI concept can also improve the temperature stability [8].

Photoluminescence (PL) measurements [9] of QW-QD TI structures reveal a nonmonotonic reduction of the tunneling efficiency with increased temperature. An energy displacement of one longitudinal optical (LO) phonon between a QW and a QD was shown [10] to enhance exciton tunneling. Optimization of the tunneling barrier thickness was studied in Ref. [11] using temperature-dependent PL.

The advantages associated with the TI process were demonstrated often, however, the exact microscopic details of the tunneling process in a TI-QD laser are not fully understood and therefore it is hard to optimize QD laser structures that realize the full potential of the TI concepts. Different aspects of TI-QD lasers were modeled previously [8,12–14]. These models were generally based on a rate equation formalism where the tunneling process serves as an additional carrier injection path with a known rate which may depend on bias [13,14]. The tunneling process itself was also studied in terms of phonon-assisted carrier transfer [15,16].

A recent paper by Michael *et al.* [17] addressed the tunneling process in a TI-QD structure by introducing a joined (hybrid) energy state that couples the first excited state of the QD with the confined quantum well (QW) injection reservoir (IW) levels and has an energy extent of roughly 5 meV. The energy levels of that structure were calculated using a $k \cdot p$ model and the scattering rates were found

*ikhanonkin@technion.ac.il

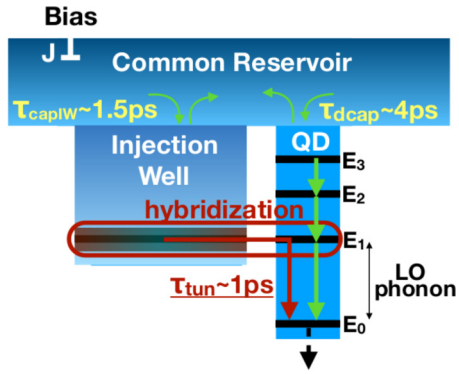

FIG. 1. Energy band structure of a TI-QD SOA for a 4.5-nm-wide IW and QDs with in-plane dimensions of 16×24 nm and a height of 3 nm. The values of the energy levels are -13.35, -41.15, -73.62, and -133.80 meV below the reservoir level. The tunneling process from the IW to the QD ground state is shown schematically. The conventional cascade carrier relaxation process from the common reservoir to the QD ground state takes $\tau_{d_{\text{cap}}} \approx 4$ ps. The tunneling injection design shortens the recovery process to $\tau_{\text{tun}} \approx 1$ ps and diminishes all other carrier capture processes to the ground state.

by conventional overlap of the various wave functions. The energy band diagram and the most important scattering rates are shown in Fig. 1. Each carrier capture event noted by a time constant τ is accompanied by a corresponding escape event. The ratio of theses two rates is dictated by detailed balance.

A detailed study of the carrier dynamics is best done in a semiconductor optical amplifier (SOA) since it is a single-pass device and therefore the responses are not masked by resonances from the end facets. A single wavelength pump-probe experimental analysis of a TI-QD SOA operating at 1300 nm was demonstrated in Ref. [18] and showed a fast recovery with a time constant of up to 10 ps.

We describe here a simulation of the broadband dynamic response of a room-temperature TI-QD SOA following a perturbation by a short pulse. Using the model described in Ref. [19] with modifications based on Ref. [20], we calculate the evolution of the inversion at every point along the SOA and across its entire gain spectrum. Additionally, we calculate the carrier dynamics in the IW. The calculations correspond to two bias levels and three pump pulse wavelengths. We find that the IW responds dynamically even for pump wavelengths which are far from the spectral region where the hybrid state dominates.

II. THEORETICAL MODEL

The theoretical investigation of ultrashort pulses propagation in a QD amplifier operating at room temperature is based on a semiclassical description of the light-matter interaction [21], solved in the dipole moment approximation. We employ a numerical finite-difference time-domain model, developed in Refs. [19,22,23], that solves Lindblad equations for the occupation probabilities of a cascade of two-level quantum systems having different transition energies that represent the inhomogeneously broadened ensemble of QDs. Simultaneously, it solves Maxwell's equation for the electromagnetic field of the propagating pulse, where the vector polarization includes contributions from the interaction with the QDs, from two-photon absorption (TPA) and its accompanying Kerr-like effect, as well as from group velocity dispersion (GVD) and the refractive index dependence on the carrier population, known as the plasma effect [23].

We simulate time- and wavelength-resolved charge carrier dynamics in the inhomogeneously broadened ensemble of QDs by a set of rate equations. The QD population is governed by relaxation from the common high-energy carrier reservoir and from tunneling that originates from the injection well. The former occur via a cascaded transition through the excited states with a time constant of around 4 ps for InAs/InP QDs having dimensions of $16 \times 24 \times 3$ nm. The reservoir is fed by an electrical dc source and by carriers generated through TPA that relax from higher-energy levels.

The set of coupled equations describing the dynamics include

$$\frac{\partial N_{\text{IW}}}{\partial t} = -\frac{N_{\text{IW}}}{\tau_{\text{IW}}} - \frac{N_{\text{IW}_{\text{targ}}}\left[1 - \exp\left(-\frac{N_{\text{IW}}}{N_{\text{IW}_{\text{targ}}}}\right)\right]}{\tau_{\text{tun}} N_{D_{\text{total}}}} \frac{V_{\text{QD}}}{V_{\text{IW}}} \sum_{i=1}^{M} N_D^i \left(1 - \rho_{11}^i\right) + \frac{V_{\text{QD}}}{V_{\text{IW}}}\left(1 - \frac{N_{\text{IW}}}{D_{\text{IW}}}\right) \sum_{i=1}^{M} 2N_D^i \frac{\rho_{11}^i}{\tau_{\text{tun}_{\text{back}}}^i} + \frac{V_{\text{res}}}{V_{\text{IW}}} \frac{N_{\text{res}}}{\tau_{\text{cap}_{\text{IW}}}}\left(1 - \frac{N_{\text{IW}}}{D_{\text{IW}}}\right) - \frac{N_{\text{IW}}}{\tau_{\text{esc}_{\text{IW}}}}\left(1 - \frac{N_{\text{res}}}{D_{\text{res}}}\right), \tag{1}$$

$$\frac{\partial P_{\text{IW}}}{\partial t} = -\frac{N_{\text{IW}}}{\tau_{\text{IW}}} + \frac{V_{\text{res}}}{V_{\text{IW}}} \frac{P_{\text{res}}}{\tau_{\text{cap}_{\text{IW}}}^h}\left(1 - \frac{P_{\text{IW}}}{D_{\text{IW}}}\right) - \frac{P_{\text{IW}}}{\tau_{\text{esc}_{\text{IW}}}^h}\left(1 - \frac{P_{\text{res}}}{D_{\text{res}}}\right), \tag{2}$$

$$\frac{\partial N_{\text{res}}}{\partial t} = \frac{\eta_i J}{qd} - \frac{N_{\text{res}}}{\tau_{\text{res}}} + \frac{V_{\text{TPA}}}{V_{\text{res}}}\left(1 - \frac{N_{\text{res}}}{D_{\text{res}}}\right) \frac{N_{\text{TPA}}}{\tau_{\text{TPA}_{\text{relax}}}} - \frac{N_{\text{res}}}{N_{D_{\text{total}}} \tau_{d_{\text{cap}}}} \frac{V_{\text{QD}}}{V_{\text{res}}} \sum_{i=1}^{M} N_D^i \left(1 - \rho_{11}^i\right) + \frac{V_{\text{QD}}}{V_{\text{res}}}\left(1 - \frac{N_{\text{res}}}{D_{\text{res}}}\right) \sum_{i=1}^{M} 2N_D^i \frac{\rho_{11}^i}{\tau_{d_{\text{esc}}}^i} - \frac{N_{\text{res}}}{\tau_{\text{cap}_{\text{IW}}}}\left(1 - \frac{N_{\text{IW}}}{D_{\text{IW}}}\right) + \frac{V_{\text{IW}}}{V_{\text{res}}} \frac{N_{\text{IW}}}{\tau_{\text{esc}_{\text{IW}}}}\left(1 - \frac{N_{\text{res}}}{D_{\text{res}}}\right), \tag{3}$$

$$\frac{P_{\text{res}}}{\partial t} = \frac{\eta_i J}{qd} - \frac{N_{\text{res}}}{\tau_{\text{res}}} + \frac{V_{\text{TPA}}}{V_{\text{res}}}\left(1 - \frac{P_{\text{res}}}{D_{\text{res}}}\right)\frac{h_{\text{TPA}}}{\tau_{\text{TPA}_{\text{relax}}}} - \frac{P_{\text{res}}}{\tau^h_{\text{cap}}}\frac{V_{\text{QD}}}{V_{\text{res}}}\frac{1}{N_{D_{\text{total}}}}\sum_{i=1}^{M} N^i_D \rho^i_{22}$$
$$+\frac{V_{\text{QD}}}{V_{\text{res}}}\left(1 - \frac{P_{\text{res}}}{D_{\text{res}}}\right)\frac{1}{\tau^h_{\text{esc}}}\sum_{i=1}^{M} 2N^i_D\left(1-\rho^i_{22}\right) - \frac{P_{\text{res}}}{\tau^h_{\text{cap}_{\text{IW}}}}\left(1 - \frac{P_{\text{IW}}}{D_{\text{IW}}}\right) + \frac{V_{\text{IW}}}{V_{\text{res}}}\frac{P_{\text{IW}}}{\tau^h_{\text{esc}_{\text{IW}}}}\left(1 - \frac{P_{\text{res}}}{D_{\text{res}}}\right), \tag{4}$$

$$\frac{\rho^i_{11}}{\partial t} = -\gamma_c \rho^i_{11} + \frac{N_{\text{res}}}{2N_{D_{\text{total}}}\tau_{d_{\text{cap}}}}\left(1-\rho^i_{11}\right) - \frac{\rho^i_{11}}{\tau^i_{d_{\text{esc}}}}\left(1 - \frac{N_{\text{res}}}{D_{\text{res}}}\right) - j\frac{\vec{\mu}\cdot\vec{E}}{\hbar}\left(\rho^i_{12} - \rho^i_{21}\right)$$
$$+\frac{N_{\text{IW}_{\text{targ}}}\left[1 - \exp\left(-\frac{N_{\text{IW}}}{N_{\text{IW}_{\text{targ}}}}\right)\right]}{\tau_{\text{tun}} 2N_{D_{\text{total}}}}\left(1-\rho^i_{11}\right) - \left(1 - \frac{N_{\text{IW}}}{D_{\text{IW}}}\right)\frac{\rho^i_{11}}{\tau^i_{\text{tun}_{\text{back}}}}, \tag{5}$$

$$\frac{\partial \rho^i_{22}}{\partial t} = \gamma_c \rho^i_{11} - \frac{P_{\text{res}}}{\tau^h_{\text{cap}}}\frac{\rho^i_{22}}{2N_{D_{\text{total}}}} + \frac{\left(1-\rho^i_{22}\right)}{\tau^h_{\text{esc}}}\left(1 - \frac{P_{\text{res}}}{D_{\text{res}}}\right) + j\frac{\vec{\mu}\cdot\vec{E}}{\hbar}\left(\rho^i_{12} - \rho^i_{21}\right), \tag{6}$$

$$\frac{\partial \rho^i_{12}}{\partial t} = -(j\omega + \gamma_h)\rho^i_{12} - j\frac{\vec{\mu}\cdot\vec{E}}{\hbar}\left(\rho^i_{11} - \rho^i_{22}\right), \tag{7}$$

$$\frac{\partial N_{\text{TPA}}}{\partial t} = I_{\text{TPA}} - \frac{N_{\text{TPA}}}{\tau_{\text{TPA}_{\text{relax}}}}\left(1 - \frac{N_{\text{res}}}{D_{\text{res}}}\right) - \frac{N_{\text{TPA}}}{\tau_{\text{TPA}_{\text{rec}}}}, \tag{8}$$

$$\frac{\partial P_{\text{TPA}}}{\partial t} = I_{\text{TPA}} - \frac{P_{\text{TPA}}}{\tau^h_{\text{TPA}_{\text{relax}}}}\left(1 - \frac{P_{\text{res}}}{D_{\text{res}}}\right) - \frac{N_{\text{TPA}}}{\tau^h_{\text{TPA}_{\text{rec}}}}. \tag{9}$$

N_{res}, P_{res}, N_{IW}, and P_{IW} are, respectively, electron and hole densities in the corresponding reservoirs and IW. J is the applied current density, and q is the electron charge. $\sum_{i=1}^{M}$ stands for the summation over all energetically similar QDs and N^i_D are their corresponding densities. ρ^i_{11} and ρ^i_{22} are the occupation probabilities of the upper and lower states and $\rho^i_{12} = (\rho^i_{21})^*$ are the coherence terms. I_{TPA}, N_{TPA}, and h_{TPA} are the TPA carrier generation rate, and the electron and hole population in the TPA levels, respectively. The definition of other variables and their corresponding values are given in Table I.

The tunneling time constant τ_{tun} is modeled as a Gaussian profile with a variance of 5 meV. Its value at the gain peak is around 1 ps. Similar to the tunneling time constant, the wavelength-dependent capture time to the QD ground state $\tau_{d_{\text{cap}}}$ is also assumed to have a Gaussian profile with a value of 4 ps far from the spectral range of the tunneling process.

The characteristic time constants of the carrier tunneling from QDs to IW, $\tau_{\text{tun}_{\text{back}}}$, escape from QD to the common reservoir, $\tau_{d_{\text{esc}}}$, and carrier escape from the IW states to reservoir, $\tau_{\text{esc}_{\text{IW}}}$, are calculated according to the principle of detailed balance.

The maximum number of carriers $N_{\text{IW}_{\text{targ}}}$ in the IW quantum well that participate in the tunneling process is limited to 4.5×10^{23} m^{-3} [17] since only the energetic bottom of the quantum well is hybridized with QDs.

The Maxwell curl equations are solved simultaneously for a transverse electric (TE) polarized propagating electromagnetic plane wave,

$$\frac{\partial E_x}{\partial z} = -\frac{\partial B_y}{\partial t}, \quad -\frac{\partial H_y}{\partial z} = \frac{\partial D_x}{\partial t}, \tag{10}$$

where E_x, H_y are the electric field and magnetic field components, respectively.

The electric displacement D_x and magnetic field B_y read as

$$D_x = \varepsilon_0 E_x + P_x, \quad B_y = \mu_0 H_y. \tag{11}$$

ε_0, μ_0 are the vacuum permittivity and permeability.

Interaction with the material perturbs the polarization P_x which includes several components,

$$P_x = P_{\text{disp}} + P_{\text{QD}} + P_{\text{plasma}} + P_{\text{TPA}} + P_{\text{Kerr}}, \tag{12}$$

which are, respectively, dispersion, radiation of the two-level systems, the plasma effect, two-photon absorption, and its accompanying Kerr-like effect.

The linear dispersion contribution to the polarization term [24] is simulated using the Lorentz model neglecting the contribution from damping,

$$P_{\text{disp}}(\omega) = \varepsilon_0 \frac{f_s \omega^2_{\text{res}} E_x}{\omega^2_{\text{res}} - \omega^2}, \tag{13}$$

where f_s is the oscillator strength and ω_{res} is the resonant frequency of the Lorentz oscillator. Those parameters can be obtained by solving coupled equations for the chosen values of the dielectric permittivity and the group velocity dispersion, which is in turn proportional to the second derivative of the square root of the dielectric permittivity.

The polarization induced by QD [19] is

$$P_{\text{QD}} = 2\mu_x \sum_{\text{ensemble}} N^i_D\left(\rho^i_{12} + \rho^{*i}_{21}\right)\Gamma, \tag{14}$$

where Γ is a confinement factor.

TABLE I. List of parameters.

$\tau_{\mathrm{cap_{IW}}}$	1.5 ps	3D to 2D electron capture time
τ_{IW}	0.4 ns	IW lifetime
$\tau^h_{\mathrm{cap_{IW}}} = \tau^h_{\mathrm{esc_{IW}}}$	0.35 ps	3D to 2D hole capture and escape times
τ_{res}	0.4 ns	Reservoir lifetime
$\tau_{\mathrm{TPA_{relax}}} = \tau^h_{\mathrm{TPA_{relax}}}$	4 ps	Relaxation time of TPA carriers to the reservoir states
$\tau_{\mathrm{TPA_{rec}}}$	0.4 ns	TPA recombination time
$\tau^h_{\mathrm{cap}} = \tau^h_{\mathrm{esc}}$	0.1 ps	3D to 0D hole capture and escape times
γ_c	2.5×10^9 s^{-1}	Density matrix diagonal elements decay rate
γ_h	2.85×10^{12} s^{-1}	Density matrix off-diagonal elements decay rate
D_{IW}	1×10^{25} m^{-3}	2D density of states
D_{res}	2×10^{25} m^{-3}	3D density of states
μ	0.5×10^{-28} C m	Dipole moment
$\frac{V_{\mathrm{res}}}{V_{\mathrm{QD}}}$	3.5	3D to 0D volume ratio
$\frac{V_{\mathrm{IW}}}{V_{\mathrm{QD}}}$	1.15	2D to 0D volume ratio
$\frac{V_{\mathrm{TPA}}}{V_{\mathrm{res}}}$	50	TPA to reservoir volume ratio
$N_{D_{\mathrm{total}}}$	4×10^{23} m^{-3}	QD density of states
η_i	0.5	Injection efficiency
L	1.5 mm	SOA length
d	18 nm	Active layer depth composed of six QD layers
W	2 μm	Ridge waveguide width
α_{TPA}	-1	α factor
β_{TPA}	70 mW^{-1}	TPA coefficient
Γ	0.0025	Confinement factor
Plasma coefficient	For gain and absorption	
C_{res}	$[0.15; 0.1] \times 10^{-26}$ m^3	Reservoir states of electrons
C_{11}	$[0.02; 0.01] \times 10^{-26}$ m^3	Upper level of QD
C_{22}	$[0.05; 0.02] \times 10^{-26}$ m^3	Lower level of QD
C_{IW}	$[0.12; 0.12] \times 10^{-26}$ m^3	IW states of electrons
$C_{h_{\mathrm{IW}}}$	$[0.15; 0.15] \times 10^{-26}$ m^3	IW states of electrons
$C_{h_{\mathrm{res}}}$	$[0.2; 0.1] \times 10^{-26}$ m^3	Reservoir states of holes

The TPA contribution to the polarization is expressed as $P_{\mathrm{TPA}} = \varepsilon_0 \chi_{\mathrm{TPA}} E_x$, where the χ_{TPA} is a function of the TPA coefficient β_{TPA}. β_{TPA} is defined by the Beer's law ($\frac{dI}{dt} = -\beta_{\mathrm{TPA}} I^2$),

$$\chi_{\mathrm{TPA}} = \frac{c^2 \varepsilon_0 n_0^2 \beta_{\mathrm{TPA}}}{2i\omega} |E_x|^2, \tag{15}$$

where c is the vacuum speed of light and n_0 is a nominal refractive index.

The real part of the refractive index is modified due to the Kerr-like effect whose contribution to the polarization is expressed using the α factor, $P_{\mathrm{Kerr}} = j\alpha\varepsilon_0 \chi_{\mathrm{TPA}} E_x$.

The contribution of the plasma effect to the polarization is $P_{\mathrm{plasma}} = \varepsilon_0 \Delta\varepsilon E$, where the carrier population in all energy levels is accounted for,

$$\Delta\varepsilon = 2C_{11} \sum_{\text{ensemble}} N_D^i \rho_{11}^i + 2C_{22} \sum_{\text{ensemble}} N_D^i \rho_{22}^i + C_{\mathrm{IW}} N_{\mathrm{IW}} + C_{h_{\mathrm{IW}}} h_{\mathrm{IW}} + C_{\mathrm{res}} N_{\mathrm{res}} + C_{h_{\mathrm{res}}} h_{\mathrm{res}}. \tag{16}$$

The values of C_{res}, C_{11}, C_{22}, C_{IW}, $C_{h_{\mathrm{IW}}}$, and $C_{h_{\mathrm{res}}}$ are listed in Table I.

III. SIMULATION PUMP-PROBE MODEL OF THE TI-QD SOA

We analyze an InAs/InP TI QD SOA operating at 1.55 μm whose epitaxial structure and dimensions are described in Ref. [25]. The gain section comprises six QD layers each having a density of 6×10^{10} cm^{-2}. The waveguide length was 1.5 mm. A hybrid state that couples the first excited state of the QD and the bottom of the IW continuum of states [17] ensures a fast carrier capture with a typical time constant of about 1 ps.

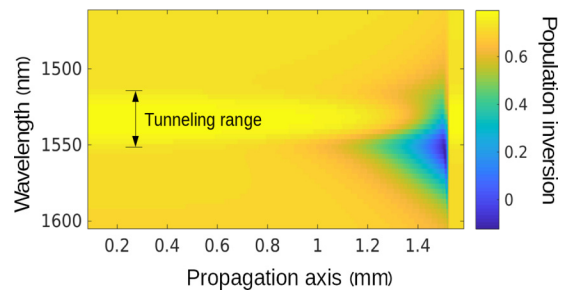

FIG. 2. Spatial evolution of the population inversions across the QD spectrum after a perturbation by a 100-pJ optical pulse at 1530 nm. The amplifier is biased at 200 mA, where it exhibits high gain across its entire gain spectrum.

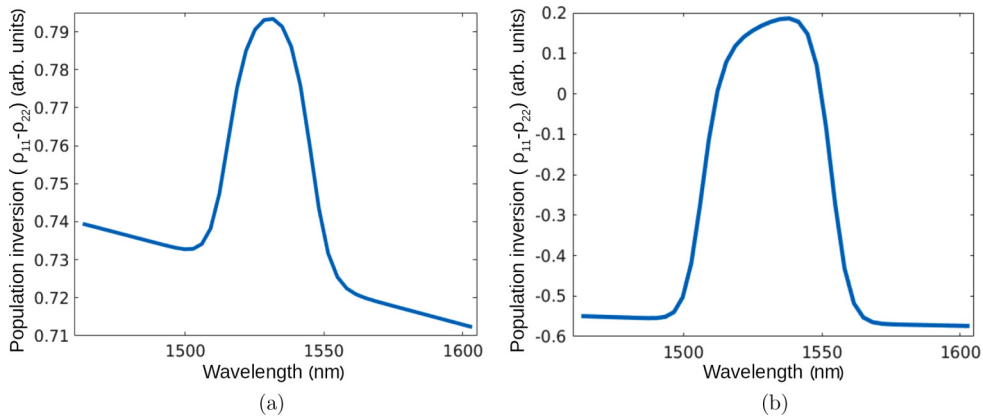

FIG. 3. Steady state inversion spectra of the QD population for a bias of (a) 200 and (b) 30 mA.

Efficient formation of the hybrid state requires a 4–5 nm wide quantum well IW, a narrow barrier between the QDs and the IW and a first QD excited state that is energetically located roughly one LO phonon from its ground state.

In addition to an accelerated replenishment rate of carriers in the QD ground state, the TI process adds an attractive feature by which it discriminates between groups of QDs and in fact filters the inhomogeneously broadened gain spectrum [26]. This is due to the finite spectral extent of the hybrid state. QDs that overlap the hybrid state spectral range are fed mainly by carriers originating in the IW with a negligible contribution from the common high-energy reservoir. In contrast, QDs with transition energies far from the tunneling range are fed mainly from the reservoir by a cascade process. This is shown in Fig. 2, which shows the population inversion (for a large bias, a 100-pJ pump pulse, and at all wavelengths) behind a pulse that propagated up to the output facet. The occupation probabilities of QDs that are spectrally close to the gain peak (1530 nm), where the tunneling process is most efficient, are high. The effective capture rate to the ground state is determined by a wavelength-dependent tunneling rate which is modeled by a Gaussian profile with a variance of 5 meV. Efficient tunneling makes the relaxation processes of direct and cascaded capture and escape, from and to the common reservoir, insignificant. However, for wavelengths far from the tunneling range, these conventional processes dominate. The two regimes are combined in the model by including a wavelength-dependent direct relaxation rate which has a Gaussian profile with an opposite sign to that of the tunneling time constant. Relaxation from the reservoir has a very long time constant, 21 ps in the tunneling spectral range, which shortens to 4 ps at the gain spectrum edges. Direct capture from the common reservoir to the ground state is determined mainly by the capture to the highest confined state. A fast cascade process (lasting a few tens of fs) follows and feeds carriers to the ground state.

The inversion profile shown in Fig. 2 is for an amplifier biased at 200 mA and a 100-pJ pulse which is injected at 1530 nm. The pulse redshifts upon propagation due to various nonlinear effects [23]. The figure shows clearly that in QDs which are close to the gain peak, the inversion recovers faster than in QDs which are far from the peak (on the long-wavelength side). This is a clear indication of the faster carrier replenishment in the spectral range where the TI process is efficient.

We investigate carrier dynamics in the TI QD SOA for two bias levels: 200 mA, where the amplifier exhibits high gain at all wavelengths, and 30 mA, where the QDs overlapping the tunneling range have gain while QDs far from the peak are absorbing. Wavelength-dependent inversion in the unperturbed steady states are shown in Fig. 3 for the two bias levels. The steady state profiles are important since the dynamical responses calculated below are normalized to them. We probe the SOA response for input pulses near the gain peak (1530 nm) and out of the tunneling range, 1480 and 1590 nm. Using the refractive index information, the spatial distribution of the charge carriers was translated to a time evolution, which reflects the commonly measured time domain response of the probe transmission [20].

IV. CARRIER DYNAMICS IN A TI-QD SOA BIASED TO THE GAIN REGIME

Time-dependent responses of the QD ground-state inversions probed at different spectral locations are shown in the Fig. 4 for a bias of 200 mA and a pump energy of 200 pJ. Each curve represents the response of a particular group of QDs. Colored curves indicate different input pump wavelengths (blue: 1480 nm; green: 1530 nm; red: 1590 nm). The traces are normalized to their respected values prior to the perturbation. The initial depth in the inversion at different pump wavelengths is directly related to the induced depletion by the corresponding pump.

Fast recovery in the QDs that spectrally overlap the tunneling region is clearly seen in Fig. 4(b). The initial saturation is deepest and the recovery is fastest for a pump wavelength of 1530 nm, but even for pump wavelengths that are far from the TI regime, the QDs near the gain peak have a significant dynamical response since even the slightest depletion of the ground state or the reservoir is easily sensed and corrected by the efficient tunneling process.

The situation is different for probes at the spectral edges. At 1465 nm [Fig. 4(a)], the inversion responds only for a pump at the same wavelength and is indifferent to pumps at lower energies. In contrast, the QDs at 1605 nm [Fig. 4(a)] exhibit some dynamical response for the higher-energy pump pulses.

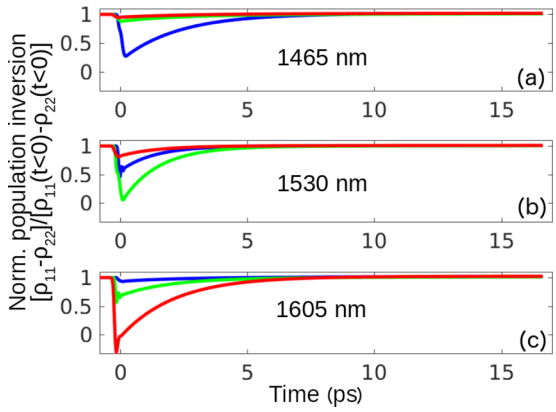

FIG. 4. Time evolution of the inversion following the perturbation at different pump wavelengths: 1480 (blue trace), 1530 (green trace), and 1590 nm (red trace). The QD ground-state inversions are normalized to their respective values prior to the perturbation. The inversions are probed at (a) −1465, (b) −1530, and (c) −1590 nm. The SOA is biased at 200 mA, where it exhibits high gain across its entire gain spectrum.

Those pump pulses redshift upon propagation and approach the tail of the long-wavelength probe region and hence affect it.

Figure 5 describes time-resolved spectra of the QD ground-state inversion. The dip in the inversion right after the interaction with the pump is slightly shifted towards long-wavelength QDs since the pump redshifts during propagation. The 1480-nm trace appears at 0 ps with no perturbation since the pump is chirped during the propagation and has not yet reached the short-wavelength QDs. Since the QDs close to 1530 nm are replenished faster, the inversion curves at 1.5 and 3 ps show a wavy profile. At very long times, all QDs recover to their steady state profiles.

Figure 6 shows the response of the electron and hole densities in the IW for the same three perturbation wavelengths. Ground-state carriers recover significantly faster when the

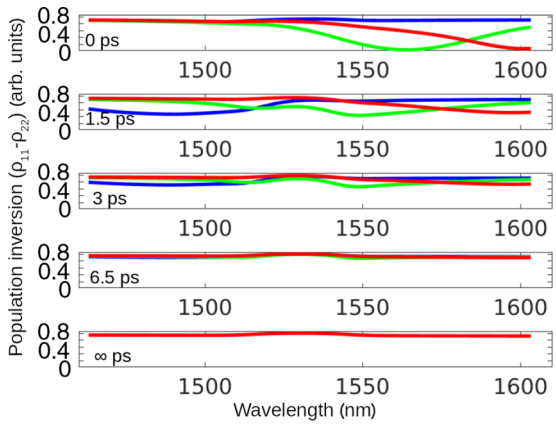

FIG. 5. Time-resolved spectral profiles of the ground-state recovery following the perturbation at different pulse wavelengths: 1480 (blue trace), 1530 (green trace), and 1590 nm (red trace). The SOA is biased at 200 mA, where it exhibits high gain across its entire gain spectrum.

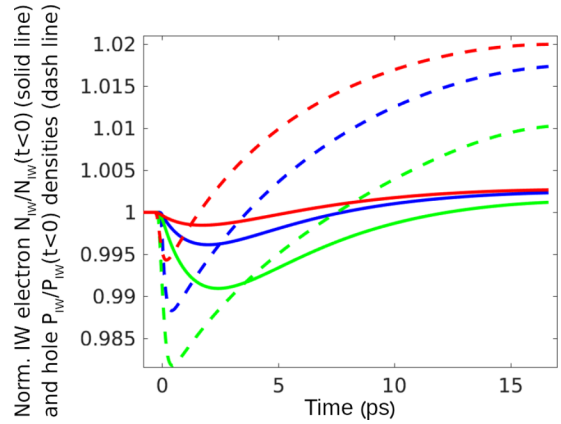

FIG. 6. Injection well electron (solid line) and hole (dashed line) densities for the three perturbations of different spectral locations. The SOA is biased at 200 mA, where it exhibits high gain across its entire gain spectrum.

perturbation is at 1530 nm, which is within the TI spectral range. The perturbation at short wavelength has a larger effect on the IW carrier density compared to the long wavelength since the redshift experience by the pump upon propagation leads to some overlap with the tunneling region.

V. CARRIER DYNAMICS IN TI-QD SOA ELECTRICALLY BIASED TO THE GAIN-ABSORPTION STATE

At a low-bias level, the TI QD SOA experiences a mixed gain-absorption state. Specifically, close to 1530 nm, the QDs exhibit gain while towards the gain spectrum edges, the QDs are absorbing. The un-normalized recovery traces in Fig. 7 show temporal responses to the three different pump wavelengths. The pump inverts the QDs located at the spectral edges when it is, correspondingly at the

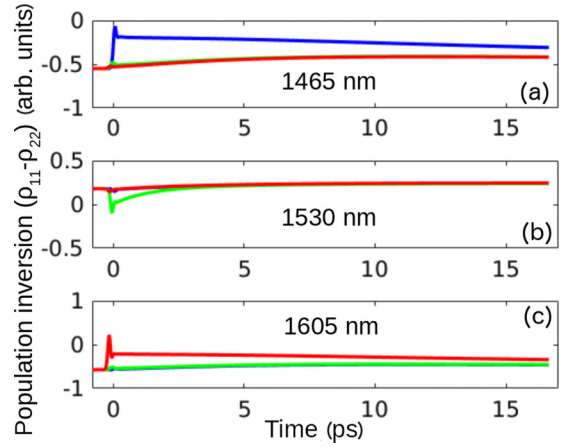

FIG. 7. Time evolution of the inversion following the perturbation at different pump wavelengths: 1480 (blue trace), 1530 (green trace), and 1590 nm (red trace). The inversions are probed at (a) −1465, (b)−1530, and (c) −1590 nm. The SOA is biased at 30 mA, where it exhibits a mixed gain-absorption state.

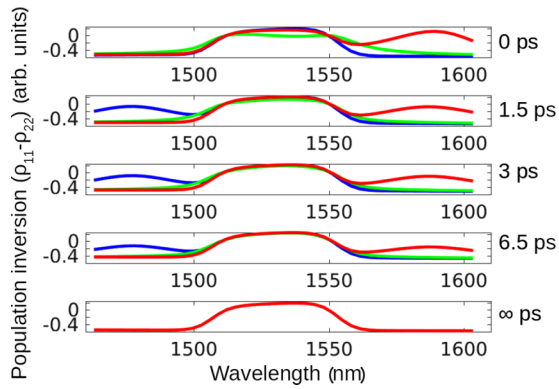

FIG. 8. Time-resolved spectral profiles of the ground-state recovery following the perturbation at different pulse wavelengths: 1480 (blue trace), 1530 (green trace), and 1590 nm (red trace). The SOA is biased at 30 mA, where it exhibits a mixed gain-absorption state.

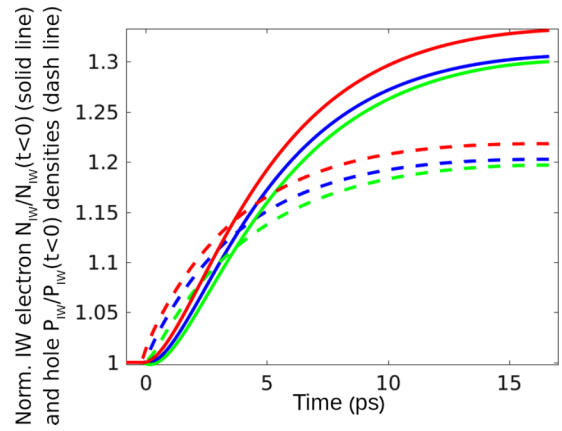

FIG. 9. Injection well electron (solid line) and hole (dashed line) densities for the three perturbations of different spectral locations. The SOA is biased at 30 mA, where it exhibits a mixed gain-absorption state.

short- and long-wavelength side of the spectrum [Figs. 7(a) and 7(c), respectively]. The responses of QDs at wavelengths far from the gain peak are all but diminished for other pump wavelengths while the QDs that participate in the tunneling process are replenished quickly [green trace in Fig. 7(b)]. An increase of the occupation probabilities to above the level prior to the pulse arrival is a result of TPA that occurs on a timescale of a few picoseconds.

Time-resolved spectral responses of the recovery are shown in Fig. 8. The QDs at the gain peak experience a small perturbation for a pump centered at 1530 nm and a fast recovery to the steady state. In contrast, the time evolution of the recovery traces in the periphery of the QD spectrum shows prolongated tails that reach an equilibrium state on a rather long timescale.

The IW electron and hole densities for the 30-mA bias level (Fig. 9) are affected mainly by TPA. The relative contribution of the TPA carriers that relax to the ground state is high compared to the equilibrium state when the bias level is low.

VI. CONCLUSION

We investigated numerically the carrier dynamics in TI QD SOA across its gain spectrum by simulating a broadband pump-probe experiment. Fast carrier replenishment in the QDs within the spectral range of the tunneling injection process is demonstrated. Moreover, we show various possibilities of amplifier operation; the amplifier can be biased in gain or in a mixed gain-absorption state. For those two different cases of amplifier operation, the effect of several perturbation wavelengths across the spectrum was analyzed.

ACKNOWLEDGMENTS

This work is partially supported by the Israel Science Foundation, Grant No. 1504/16. M.L., S.M., and F.J. acknowledge funding from the DFG and a grant for CPU time from the HLRN (Hannover/Berlin).

[1] R. Tucker, J. Lightwave Technol. **3**, 1180 (1985).
[2] K. Hall, G. Lenz, A. Darwish, and E. Ippen, Opt. Commun. **111**, 589 (1994).
[3] A. Mecozzi and J. Mørk, J. Opt. Soc. Am. B **14**, 761 (1997).
[4] O. Buchinsky, M. Blumin, R. Sarfaty, D. Fekete, M. Orenstein, and G. Eisenstein, Appl. Phys. Lett. **70**, 1787 (1997).
[5] H. C. Sun, L. Davis, S. Sethi, J. Singh, and P. Bhattacharya, IEEE Photonics Technol. Lett. **5**, 870 (1993).
[6] S. Ghosh, S. Pradhan, and P. Bhattacharya, Appl. Phys. Lett. **81**, 3055 (2002).
[7] S. Bhowmick, M. Z. Baten, T. Frost, B. S. Ooi, and P. Bhattacharya, IEEE J. Quantum Electron. **50**, 7 (2014).
[8] L. V. Asryan and S. Luryi, IEEE J. Quantum Electron. **37**, 905 (2001).
[9] Y. I. Mazur, B. Liang, Z. M. Wang, D. Guzun, G. Salamo, Z. Y. Zhuchenko, and G. Tarasov, Appl. Phys. Lett. **89**, 151914 (2006).
[10] P. Podemski, R. Kudrawiec, J. Misiewicz, A. Somers, J. Reithmaier, and A. Forchel, Appl. Phys. Lett. **89**, 061902 (2006).
[11] C. Jin, S. Ohta, M. Hopkinson, O. Kojima, T. Kita, and O. Wada, Appl. Phys. Lett. **96**, 151104 (2010).
[12] P. Bhattacharya, J. Singh, H. Yoon, X. Zhang, A. Gutierrez-Aitken, and Y. Lam, IEEE J. Quantum Electron. **32**, 1620 (1996).
[13] D. Gready and G. Eisenstein, IEEE J. Quantum Electron. **47**, 944 (2011).
[14] D. Gready and G. Eisenstein, IEEE J. Quantum Electron. **46**, 1611 (2010).
[15] S.-W. Chang, S.-L. Chuang, and N. Holonyak, Jr., Phys. Rev. B **70**, 125312 (2004).
[16] A. Mielnik-Pyszczorski, K. Gawarecki, and P. Machnikowski, Phys. Rev. B **91**, 195421 (2015).
[17] S. Michael, M. Lorke, M. Cepok, C. Carmesin, and F. Jahnke, arXiv:1803.03787.

[18] J. Pulka, T. Piwonski, G. Huyet, J. Houlihan, E. Semenova, A. Lematre, K. Merghem, A. Martinez, and A. Ramdane, Appl. Phys. Lett. **100**, 071107 (2012).

[19] A. Capua, O. Karni, and G. Eisenstein, IEEE J. Sel. Top. Quantum Electron. **19**, 1 (2013).

[20] I. Khanonkin, A. Mishra, O. Karni, V. Mikhelashvili, S. Banyoudeh, F. Schnabel, V. Sichkovskyi, J. Reithmaier, and G. Eisenstein, AIP Adv. **7**, 035122 (2017).

[21] A. Icsevgi and W. Lamb, Jr., Phys. Rev. **185**, 517 (1969).

[22] A. K. Mishra, O. Karni, and G. Eisenstein, Opt. Express **23**, 29940 (2015).

[23] O. Karni, A. K. Mishra, G. Eisenstein, and J. P. Reithmaier, Phys. Rev. B **91**, 115304 (2015).

[24] N. Suzuki, J. Lightwave Technol. **25**, 2495 (2007).

[25] S. Bauer, V. Sichkovskyi, and J. P. Reithmaier, J. Cryst. Growth **491**, 20 (2018).

[26] P. Bhattacharya, S. Ghosh, S. Pradhan, J. Singh, Z.-K. Wu, J. Urayama, K. Kim, and T. B. Norris, IEEE J. Quantum Electron. **39**, 952 (2003).